RSC Advances

ROYAL SOCIETY OF CHEMISTRY

www.rsc.org/advances

RSC Advances

PAPER

An easy and novel approach to prepare Fe_3O_4-reduced graphene oxide composite and its application for high-performance lithium-ion batteries

Received 00th January 20xx,
Accepted 00th January 20xx

DOI: 10.1039/x0xx00000x

www.rsc.org/

Xianhong Chen[*ab], Xin Lai[b], Jinhui Hu[*c], Long wan[b]

Abstract: In this paper, the ferroferric oxide-reduced graphene oxide (Fe_3O_4-rGO) composite is prepared by a facile one-step solvothermal method in which the reduction process of graphene oxide (GO) into rGO was accompanied by the generation of Fe_3O_4 particles without additional molecular linkers and further process. The X-ray diffraction (XRD) pattern of the composite reveals the presence of face-centered cubic Fe_3O_4. Fourier transform infrared (FTIR) and Raman spectroscopy demonstrate that the GO is reduced to rGO in the solvothermal process. The Scanning electron microscopy (SEM) images of the composite indicate that the porous Fe_3O_4 particles are anchored on rGO sheets with an average diameter of ~160 nm, and the amount of Fe_3O_4 is about 80.7 wt.% by thermo-gravimetric (TG) analysis. The Fe_3O_4-rGO composite exhibits improved cycling stability and rate performances as a potential anode material for high-performance lithium ion batteries (LIBs). It has specific capacities for the first discharge and charge of 1912 and 1450 mAh·g^{-1}, respectively, which is higher than that of pure Fe_3O_4. Meanwhile, it shows good capacity retention of 1031 mAh·g^{-1} after 50 cycles, still 84% of the initial capacity. This outstanding electrochemical behaviour can be attributed to the increased electrical conductivity and mechanical stability of Fe_3O_4 by rGO support during the charging and discharging processes.

Keywords: graphene; Fe_3O_4; composite; anode; Lithium-ion batteries

1. Introduction

Materials for electrodes of lithium ion batteries (LIBs) have been intensely explored due to the demand of renewable energy sources for a wide spectrum of applications, from portable electronics to electrical vehicles.[1] Anode materials play crucial roles in the performance of lithium batteries. Nowadays, graphite (as the negative electrode)[2] is widely used as the anode material of LIBs in the market. However, the main disadvantages of graphite are low theoretical capacity (372 mAh·g^{-1})[3] and dendrite formation with lithium leading to short circuit at higher current rate operation. Therefore, it cannot meet the increasing demands in higher energy density, faster charge/discharge rate, and more durable cycling performance. To enhance the battery performance, alternative anode materials are required. In addition, reducing the cost, eco-friendly and improving the safety of the electrode materials are essential for their viable use. Over the past decades, significant achievements have been gained in developing new high-performance electrode materials for next-generation LIBs. It is reported that metal, metal oxides and metal sulfides are extensively investigated as possible alternative to replace the graphite anode.[4-11] The ferriferrous oxide (Fe_3O_4) has been considered one of the most promising electrode materials because of its high theoretical capacity (924 mAh·g^{-1}), low cost, nontoxicity, good chemical stability and environmental friendliness.[12-14] In addition, Fe_3O_4 has a broad potential electrochemical window up to 1.2 V in aqueous electrolyte, which is conducive to improving the energy density.[14,15] However, a significant restriction for Fe_3O_4 is its poor capacity retention, low electronic conductivity and poor cycling performance.[13,16] Recently, some researchers found that the above problems are partly attributed to the large volume changes and aggregation of metal oxides particles repeated lithium uptake and removal reactions, which causes crumbling and cracking of the electrode, leading to electrical disconnection from current collectors.[7,8,17] The aggregation of particles leads to significant reduction in active surface area, while at the same time, the electrical contacts with the carbon-black component also deteriorate, resulting in rapid and significant capacity fading.[18] One generally accepted strategy to alleviate these problems is to prepare micro/nanometre Fe_3O_4/carbon composites by loading micro/nanometre-sized Fe_3O_4 onto a carbon-based matrix[19-

[a]College of Packaging and Materials Engineering, Hunan University of Technology, Zhuzhou, P. R. China. E-mail: xianhongchen@hnu.edu.cn; Tel: +86 0731-22183429

[b]College of Materials Science and Engineering, Hunan University, Changsha, P. R. China

[c]People's Hospital of Hunan Province, Changsha, P.R. China. E-mail: 798076678@qq.com; Tel: +86 0731-83929027

[23] because reducing the particle size will increase the surface to volume ratio and that would decrease the volume changes during the Li-ion insertion and extraction.

Graphene, a new allotrope of carbon, has drawn tremendous scientific interest for energy-storage application due to its excellent electrical conductivity ($\sigma = 1\times10^6$ $ohm^{-1}cm^{-1}$),[24] high surface area (2300 $m^2\cdot g^{-1}$),[13] chemical tolerance and broad electrochemical window.[25-27] These unique properties of graphene have attracted much attention for the application in energy storage systems. Graphene and graphene-based composites have been reported as anode materials for LIBs.[28,29] The porous graphene[30] could provide a void space against the volume changes of the Fe_3O_4 during Li^+ insertion/extraction process and prevent the aggregation of Fe_3O_4.[31] Therefore, it is believed that such Fe_3O_4-graphene composite could possess large reversible specific capacity, good rate capability and long cycling life. Sathish et al.[9] have showed that Fe_3O_4/graphene composite, synthesized by hydrothermal method, posses high reversible capacities of about 900 $mAh\cdot g^{-1}$ after 50 cycles. Wang et al.[16] have prepared the Fe_3O_4-graphene with 3D laminated structure, which exhibits a stable capacity of about 650 $mAh\cdot g^{-1}$ with on noticeable fading for up to 100 cycles.

Currently, various chemistry-based methods have been reported to produce Fe_3O_4-graphene composite, including in situ approach and ex situ approach.[32] For the ex situ approach, Fe_3O_4 was produced in advance and then attached to the surface of graphene via linking agents.[33] Chen et al.[24] have obtained graphene encapsulated hollow Fe_3O_4 nanoparticle by a two step process involving hydrothermal synthesis and postsynthesis self-assembly. Nevertheless, this approach is relatively complicated, involving additional steps. On the other hand, in situ approach is more widely used in the produce of Fe_3O_4-graphene composite.[34-36] The main advantage of this approach is that the protecting surfactant or linker molecules could be avoided, which may leads to an easy experimental procedure. Studies show that composites prepared through in situ approach usually leads to better performance for LIBs than that of ex situ method.[14,32,37] Another advantage of in situ approach is that a variety of chemical and physical synthesis techniques could be used. Hydrothermal/solvothermal methods have been widely applied for the preparation of graphene-inorganic composites. The advantage of the two methods include the mild conditions, the ability to prepare large crystals with high quality and the potential for industrial application.[32,33]

Herein, we report a one-step solvothermal route for preparing Fe_3O_4-reduced graphene oxide (Fe_3O_4-rGO) composite directly from graphene oxide (GO) and ferrous chloride ($FeCl_2\cdot4H_2O$) in the presence of hydrazine hydrate, schematically illustrated in Fig. 1. Through this simple in situ method, the reduction of GO, the formation and the deposition of Fe_3O_4 particles on rGO sheets by directly anchored way occur simultaneously without additional molecular linkers and further process. The electrochemical performance of Fe_3O_4-rGO composite as an anode materials for LIBs has been investigated and compared with pure Fe_3O_4. It is found that the Fe_3O_4-rGO composite exhibits excellent capacitive behaviour in terms of high specific capacity, good rate capability and cycling performance because the rGO sheets can not only efficiently buffer the volume change and prevent the aggregation of Fe_3O_4 particles during charging and discharging processes but also preserve the high electrical conductivity of the overall electrode.

2. Experimental

2.1. Materials

Natural flake graphite powder (99%) was purchased from Qingdao Henglide Graphite Co., Ltd. and used without any further treatment. $NaNO_3$, $KMnO_4$ and ethylene glycol (EG) were obtained from Tianjin hengxing Chemical Co., Ltd.. H_2O_2 and hydrazine hydrate were supplied by Xilong Chemical Co., Ltd.. $FeCl_2\cdot4H_2O$ were purchased from Tianjin jinfeng Chemical Co., Ltd.. All other solvents and reagents were obtained from commercial sources and used as received.

2.2. Sample preparation

(1) Preparation of GO/EG solution

GO was synthesized from natural graphite powder by a modified Hummers method.[38] In detail, 5 g graphite powder and 2.5 g $NaNO_3$ were placed in a 1000 ml flask, then 115 ml concentrated H_2SO_4 was added. The flask was immersed in an ice water bath. Subsequently, 15 g $KMnO_4$ was slowly added to the flask and kept stirring for 2 h. The flask was transferred into a 35 ^oC water bath and stirred for 3 h. 230 ml deionized water was added and the resulting solution was stirred for 30 min while the temperature was raised to 95 ^oC. After the addition of 345 ml deionized water and 45 ml 30% H_2O_2 solution, the color of the mixture changed to bright yellow. The mixture was filtered and washed with 5% HCl and deionized water several times to remove other ions then dried at 60 ^oC under vacuum. The obtained graphite oxide was dissolved in EG and then treated by ultrasonication for 12 h. A homogeneous brown GO/EG solution was obtained after the removal of the insoluble substrate by centrifugation (5000 rpm, 10 min), and its concentration was measured to be about 2.1 g/L.

(2) Preparation of Fe_3O_4-rGO composite and pure Fe_3O_4

0.99 g $FeCl_2\cdot4H_2O$, 1 g polyethylene glycol (PEG 1000) and 20 ml EG were placed in a beaker to form a homogeneous solution, then 15 ml GO/EG solution was added. After ultrasonication for 15 min, 0.5 ml hydrazine hydrate was added by dropwise to the beaker while the mixture stirred for 10 min. The above mixture was then transferred into a 50 ml Teflon-lined autoclave and maintained at 180 ^oC for 8 h, then cooled to room temperature. The obtained black product was washed with a large amount of deionized water and then dried at 60 ^oC in a vacuum oven overnight. For comparison, the pure Fe_3O_4 was also prepared by the same approach without adding GO.

2.3. Characterization

The X-ray diffraction (XRD) analysis was carried out on a Siemens D5000 diffractometer with the Cu Kα radiation (λ = 1.54056 Å) in reflection mold from 5° to 80° of 2θ angle. Fourier transform infrared spectroscopy (FTIR) measurements were recorded on a Nicolete 380 spectrometer using pressed KBr pellets to test the chemical bonding of the products from 400 to 4000 cm^{-1}. Raman spectroscopy measurements were carried out on a laser confocal Raman spectrometer (JOBINYVON Labram-010, 632.8 nm excitation). Thermo-gravimetric (TG) analysis was performed on a STA 447 instrument under an air atmosphere with a heating rate of 10 ^oC/min from room temperature to 800 ^oC. Scanning electron microscopy (SEM) images were recorded by JSM–6700F field-emission microscope.

The electrochemical experiments were measured using the CR2016-type coin cells. The working electrodes were fabricated by mixing 80 wt.% active materials (Fe_3O_4 or Fe_3O_4-rGO, without heat treatment after preparation), 10 wt.% acetylene black and 10 wt.% polyvinylidene difluoride (PVDF) binder in an appropriate amount of N-methyl-2-pyrrolidone (NMP) as solvent. The resultant slurry was uniformly spread on Cu foil by a blade, dried at 120 ^oC in a vacuum oven and pressed under a pressure of 1.0 MPa. The Cu foil loaded with active materials was cut into circular sheets with a diameter of 12 mm, and the weight of active materials was measured to be about 1 mg. The cells were assembled in an argon-filled glove box using those sheets as the working electrode. Cyclic voltammograms (CV) experiments of the cells were carried out by the CHI660e instrument at a scanning rate of 0.2 $mV \cdot s^{-1}$. Galvanostatic cycling experiments were performed on a LAND CT2001A battery test system in the voltage range of 0.01-3.00 V versus Li^+/Li at 25 ^oC.

3. Results and Discussion

3.1. Characterization of the Fe_3O_4-rGO composite

3.1.1. XRD analysis

The XRD patterns of GO, rGO, Fe_3O_4 and Fe_3O_4-rGO composite are showed in Fig. 2. The diffraction peak of GO sample shows a sharp diffraction peak at around 2θ = 11.2° (Fig. 2a). After reduction, this diffraction peak for GO has disappeared, while a new broad peak has arisen at 2θ = 23° (Fig. 2b). This broad peak is a typical pattern of amorphous carbon structure, indicating a short range order in stacked rGO layers.[39] As for Fe_3O_4 (Fig. 2c), the characteristic peaks such as (220), (311), (400), (422), (511) and (440) planes are observed at 2θ = 30.1°, 35.4°, 43.0°, 53.4°, 56.9° and 62.6°, respectively. These peaks match well with those of the crystalline face-centered cubic Fe_3O_4 (JCPDS 19-0629).[40] There are no apparent movement for the peaks of Fe_3O_4-rGO composite (Fig. 2d), compared with that of pure Fe_3O_4. Besides, it is worth noting that a diffraction hump appears in the range of 21°-25°, which originates from rGO (inset of Fig. 2). This indicates that the GO is reduced to rGO during the in situ solvothermal process. However, it could also be watched that the intensity of rGO diffraction peak in Fe_3O_4-rGO composite is very weak because of its high disorder degree and low content.

3.1.2. FTIR spectra analysis

To further investigate the reduction of GO, FTIR spectra of graphite, GO and Fe_3O_4-rGO composite are shown in Fig. 3. For GO (Fig. 3b), some new functional groups appear after the oxidation of graphite (Fig. 3a), including peaks at 1053 cm^{-1} (C-O-C stretching vibration of epoxide), 1224 cm^{-1} (C-O stretching vibration of C-OH) and 1709 cm^{-1} (C=O stretching of carbonyl groups). This agrees well with the reported reference.[41] The FTIR spectra of Fe_3O_4-rGO composite shows significant differences from that of GO. The intense peak at 576 cm^{-1} corresponds to the vibration of Fe-O bonds in the crystalline lattice of Fe_3O_4.[42] All these absorption peaks related to oxidized groups of GO are almost vanished, indicating that GO has been reduced to rGO by hydrazine hydrate. While the new bank is observed between 1500-1600 cm^{-1}, attributed to the aromatic skeletal C=C stretching vibration of rGO.[43] These results obtained from FTIR spectrum are in good agreement with the XRD analysis.

3.1.3. Raman spectra analysis

In addition, significant structural changes of the carbon framework occurring during the reduction are also reflected in their Raman spectra (Fig. 4). The Raman spectrum of GO (Fig. 4a) contains D band (~1334 cm^{-1}, for A_{1g} phonon of carbon sp^3 atoms from defects and boundaries of lattice) and G band (~1591 cm^{-1}, E_{2g} phonon of carbon sp^2 atoms).[44] It can be observed that there are no change of the positions and shapes of the D band and G band of rGO in Fe_3O_4-rGO composite (Fig. 4b), compared with GO. The intensity ratio of D band and G band (I_D/I_G) is used to evaluate the ordered and disordered crystal structures of carbon.[45] The I_D/I_G ratio is 1.0 for GO, and 1.7 for Fe_3O_4-rGO composite. The change in I_D/I_G ratios explains the fact that the reduction of GO leads to smaller but more numerous sp^2 domains in the carbon.[19] While the presence of defects on the surface of rGO could be applied to store an extra number of lithium ions.[46]

3.1.4. TG analysis

To quantify the amount of rGO and Fe_3O_4 components in the composite, a typical TG analysis was carried out in air. Fig. 5 shows the TG profile of Fe_3O_4-rGO composite along with those of pure rGO and Fe_3O_4. For rGO (Fig. 5a), an abrupt weight loss occurs between 300 ^oC and 600 ^oC, attributed to the oxidation of rGO. And the weight drops to nearly null after 600 ^oC. While the weight of pure Fe_3O_4 (Fig. 5c) remains almost stable in this temperature range. A small mass gain between 200 ^oC and 400 ^oC appears in the profile, owing to the oxidation of Fe_3O_4 by gradually heating in air.[47] It can be seen from Fig. 5b, Fe_3O_4-rGO composite shows rapid mass loss between 400 ^oC and 590 ^oC. Calculated from the weight losses of rGO and the mass gains of the oxidation of Fe_3O_4, the Fe_3O_4 contents of the sample is about 80.7 wt.%. It is clear that the amount of rGO in the composite is about 19.3 wt.%.

3.1.5. SEM images

To investigate the morphology and structure of the products, SEM images were taken for the GO, Fe_3O_4 and Fe_3O_4-rGO composite. Fig. 6a shows the typical sheet-like structure of GO, revealing a crumpled and rippled structure, as a result of deformation upon the exfoliation and restacking process. Fig. 6b presents a typical SEM image of Fe_3O_4 particles. The particles are spherical in shape and nearly monodisperse in size with an average diameter of ~160 nm. Furthermore, the Fe_3O_4 particle is composed of several small nanocrystals with a rough surface and obvious pores can be found. For Fe_3O_4-rGO composite, it can be watched from Fig. 6c,d that the porous Fe_3O_4 particles are anchored on the layered and wrinkled rGO sheets without apparent aggregation. Furthermore, we find that even after a long time of ultrasonication, the particles are still firmly anchored on the surface of rGO sheets uniformly (Fig. 7), indicating the strong interaction between Fe_3O_4 and rGO. Such almost perfect combination prevents the agglomeration of particles, also enables fast electron transport through the underlying rGO layers to Fe_3O_4 particles, ensuring the efficient electrochemical performance.[19] On the other hand, the porous structure can not only increase the contact area between electrode and electrolyte, but also provide more space for the volume change during charge/discharge process when the Fe_3O_4-rGO composite is used as electrode materials.[48]

3.2 Electrochemical Properties of Fe_3O_4-rGO composite

3.2.1. Cyclic voltammetry (CV)

To identify all of the electrochemical reactions, CV was conducted on the cell of Fe_3O_4-rGO composite in the 0.0-3.0 V range and a

scan rate of 0.2 mV·s^{-1} (Fig. 8). In the first cycle, the peaks in the cathodic scan at 0.83 V and 0.63 V could be attributed to the two steps of the reduction reactions of Fe_3O_4 to Fe^0 [Eqs.(1) and (2)] and the irreversible decomposition of the electrolyte.

$$Fe_3O_4 + 2Li^+ + 2e^- \rightarrow Li_2(Fe_3O_4) \quad (1)$$

$$Li_2(Fe_3O_4) + 6Li^+ + 6e^- \rightarrow 3Fe^0 + 4Li_2O \quad (2)$$

Meanwhile, the anodic peaks at 1.69 V and 1.81 V in the anodic process corresponds to the reversible oxidation of Fe^0 to Fe_3O_4. This agrees well with the earlier study.[16] The redox reaction of Fe could support 8 mols of Li^+ insertion/extraction per formula weight of Fe_3O_4, providing a higher reversible lithium storage capacity. Apparently, the peak intensity drops significantly in the second cycle, indicating the occurrence of some irreversible reactions and the formation of the solid electrolyte interface (SEI) film.[46] It can be found by further comparison that the difference of the peak current and the integrated area intensity between the 2nd and 3rd cycle is very small, indicating that there is almost no capacity loss during charge process.

3.2.2. Charge-discharge profiles

To demonstrate the potential of Fe_3O_4-rGO composite as anode material for LIBs, we conducted a preliminary investigation on the electrochemical performance of this material toward Li^+ insertion/extraction comparing with that of pure Fe_3O_4 under the same electrochemical conditions. Fig. 9 shows the charge-discharge profiles of Fe_3O_4 (Fig. 9a) and Fe_3O_4-rGO (Fig. 9b) electrodes from first to fifth cycles at a current density of 92.4 mA·g^{-1}. In the first discharge step, both of them present an extended voltage plateau at about 0.80 V, which is attributed to the reduction of Fe_3O_4. The sloping curve from 0.80 V to 0.01 V could be mainly attributed to the formation of the SEI film, which is typical characteristic of voltage trends for the Fe_3O_4 electrode.[30] The first discharge and charge capacities are 1912 and 1450 mAh·g^{-1} for Fe_3O_4-rGO electrode, higher than those of Fe_3O_4 electrode (1342 and 991 mAh·g^{-1}). The initial capacity loss may be caused by the formation of SEI film and the reaction of Li^+ with oxygen-containing functional groups remaining unreduced on the surface of rGO.[49] In the following cycles, the capacity of Fe_3O_4 electrode decreases with each cycle while Fe_3O_4-rGO electrode shows better capacity retention. After five discharge-charge cycles, the capacity of Fe_3O_4 electrode rapidly drops to 775 mAh·g^{-1} with a lower coulombic efficiency of 92.3%. By contrast, the Fe_3O_4-rGO electrode exhibits a high capacity of 1547 mAh·g^{-1}, and the coulombic efficiency rises rapidly from 75.8% in the first cycle to 98.1% in the fifth one. These results imply that Fe_3O_4-rGO composite is electrochemically stable, which makes it a promising anode materials for LIBs.

3.2.3. Rate performance

To further investigate the electrochemical performance of the Fe_3O_4 and Fe_3O_4-rGO electrodes, the rate capabilities of the samples operated at different current densities between 92.4 and 4620 mA·g^{-1} are shown in Fig. 10. It can be watched that both of the electrodes have significant capacities fading with the increasing of current densities. Obviously, Fe_3O_4-rGO electrode (Fig. 10b) shows higher capacities than those of Fe_3O_4 electrode (Fig. 10a) at all current densities. For example, Fe_3O_4-rGO electrode keeps a capacity of 1628 mAh·g^{-1} after the 5th cycle at a current density of 92.4 mA·g^{-1}, whereas that of Fe_3O_4 electrode drops to 775 mA·g^{-1}. At the higher current density of 4620 mA·g^{-1}, the capacity of Fe_3O_4-rGO electrode is still as high as 480 mAh·g^{-1}, while that of the Fe_3O_4 electrode rapidly drops to nearly null. Remarkably, when the current density returns to the initial 92.4 mA·g^{-1} after 30 cycles, the capacity of Fe_3O_4-rGO electrode almost returns to the initial capacity, which illustrates that the structure of anode materials is almost no damaged. Those results indicate that Fe_3O_4-rGO electrode has better capacity retention at high current rate and cycling stability than Fe_3O_4 electrode.

3.2.4. Cycling behaviour

Fig. 11 shows the cycling behaviour of the Fe_3O_4 and Fe_3O_4-rGO electrodes at a current density of 924 mA·g^{-1}. Obviously, Fe_3O_4-rGO electrode exhibits a better cycle performance than Fe_3O_4 electrode. Although the discharge capacity of Fe_3O_4 electrode (Fig. 11a) is 1034 mAh·g^{-1} for the first cycle, the capacity decreases rapidly for the first five cycles, and reaches 589 mAh·g^{-1}. After that, the capacity decreases slowly and finally reaches 226 mAh·g^{-1} after 50 cycles, which is only about 21% of the initial capacity, indicating poor capacity retention. By contrast, the capacities of Fe_3O_4-rGO electrode (Fig. 11b) decreases much slowly from the very first. After 5 cycles, the capacity decreases to 1225 mAh·g^{-1}, which remains almost unchanged compared with the first capacity (1234 mAh·g^{-1}). And a stable higher capacity of 1031 mAh·g^{-1} can be sustained after 50 cycles, still 84% of the initial capacity, which is much higher than that of similar reports.[12,50] These results imply that Fe_3O_4-rGO electrode has a higher capacity and better capacity retention than Fe_3O_4 electrode.

4. Conclusions

The Fe_3O_4-rGO composite was prepared directly from GO and $FeCl_2·4H_2O$ through a facile one-step solvothermal method. The results of XRD, FTIR and Raman indicate the presence of Fe_3O_4 and rGO in the composite. The SEM images show that the porous Fe_3O_4 particles are anchored on rGO sheets with an average diameter of ~160 nm. The composite exhibits improved cycling stability and rate performances as a potential anode material for LIBs. It has specific capacities for the first discharge and charge of 1912 and 1450 mAh·g^{-1}, respectively. The rate performance of the Fe_3O_4-rGO electrode shows high reversible capacities at high rates due to the high conductive rGO support. A stable high reversible specific capacity (1031 mAh·g^{-1}) of Fe_3O_4-rGO electrode can be sustained after 50 cycles, still 84% of the initial capacity. The total specific capacities of Fe_3O_4-rGO electrode are higher than those of Fe_3O_4 electrode because rGO in composite can not only efficiently buffer the volume change and prevent the aggregation of Fe_3O_4 particles during charging and discharging processes but also preserve the high electrical conductivity of the overall electrode. Considering the advantages of efficiency, simplicity and low-cost, this new approach may open up new avenues for preparing Fe_3O_4-rGO composite with improved reversible capacity and cyclic stability for practical applications in the fields of high-performance LIBs.

Acknowledgment

This work was supported by the National Natural Science Foundation of China (No. 51374102) and the Hunan Provincial Natural Science Foundation of China (No. 14JJ5020).

Notes and References

1. Y. Wu, Y. Wei, J. P. Wang, K. L. Jiang and S. S. Fan, *Nano Lett.*, 2013, **13**, 818-823.
2. M. V. Reddy, C. T. Cherian, K. Ramanathan, K. C. W. Jie, T. Y. W. Daryl, T. Y. Hao, S. Adams, K. P. Loh and B. V. R. Chowdari, *Electrochim. Acta*, 2014, **118**,75-80.
3. M. H. Liang and L. J. Zhi, *J. Mater. Chem.*, 2009, **19**, 5871-5878.
4. Y. Jin, H. Munakata, N. Okada and K. Kanamura, *J. Nanomater*, 2013, **2013**, Article ID 937019.
5. M. V. Reddy, K. Y. H. Kenrick, T. Y. Wei, G. Y. Chong, G. H. Leong and B.V. R. Chowdari, *J. Electrochem. Soc.*, 2011, **158**, 1423-1430.
6. C. T. Cherian, J. Sundaramurthy, M. V. Reddy, P. S. Kumar, K. Mami, D. Pliszka, C. H. Sow, S. Ramakrishna and B. V. R. Chowdari, *Appl. Mater. Interfaces*, 2013, **5**, 9957-9963.
7. J. Fan, T. Wang, C. Z. Yu, B. Tu, Z. Y. Jiang and D. Y. Zhao, *Adv. Mater.*, 2004, **16**, 1432-1436.
8. F. M. Zhan, B. Y. Geng and Y. J. Guo, *Chem. Eur. J.*,2009, **15**, 6169-6174.
9. M. Sathish, T. Tomai and I. Honma, *J. Power Sources*, 2012, **217**, 85-91.
10. M. V. Reddy, Y. Cai, J. H. Fan, K. P. Loh and B. V. R. Chowdari, *RSC Adv.*, 2012, **2**, 9619-9625.
11. Y. Z. Jiang, M. J. Hu, D. Zhang, T. Z. Yuan, W. P. Sun, B. Xu and M. Yan, *Nano Energy*, 2014, **5**, 60-66.
12. L. Wang, Y. Yu, P. C. Chen, D. W. Zhang and C. H. Chen, *J. Power Sources*, 2008, **183**, 717-723.
13. A. P. Hu, X. H. Chen, Y. H. Tang, L. Yang, H. H. Xiao and B. B. Fan, *Mater. Lett.*, 2013, **91**, 315-318.
14. Q. T. Qu, S. B. Yang and X. L. Feng, *Adv. Mater.*, 2011, **23**, 5574-5580.
15. T. Qi, J. J. Jiang, H. C. Chen, H. Z. Wan, L. Miao and L. Zhang, *Electrochim. Acta*, 2013, **114**, 674-680.
16. J. Z. Wang, C. Zhong, D. Wexler, N. H. Idris, Z. X. Wang, L. Q. Chen and H. K. Liu, *Chem. Eur. J.*, 2011, **17**, 661-667.
17. W. Y. Li, L. N. Xu and J. Chen, *Adv. Funct. Mater.*, 2005, **15**, 851-857.
18. J. Chen, L. N. Xu, W. Y. Li and X. L. Gou, *Adv. Mater.*, 2005, **17**, 582-586.
19. J. Su, M. H. Cao, L. Ren and C. W. Hu, *J. Phys. Chem. C*, 2011, **115**, 14469-14477.
20. C. N. He, S. Wu, N. Q. Zhao, C. S. Shi, E. Z. Liu and J. J. Li, *ACS Nano*, 2013, **7**, 4459-4469.
21. G. M. Zhou, D. W. Wang, F. Li, L. L. Zhang, N. Li, Z. S. Wu, L. Wen, G. Q. Lu and H. M. Cheng, *J. Am. Chem. Soc.*, 2010, **22**, 5306-5313.
22. G. Chen, M. Zhou, J. Catanach, T. Liaw, L. Fei, S. G. Deng and H. M. Luo, *Nano Energy*, 2014, **8**, 126-132.
23. S. Z. Liang, X. F. Zhu, P. C. Lian, W. S. Yang and H. H. Wang, *J. Solid State Chem.*, 2011, **184**, 1400-1404.
24. D. Y. Chen, G. Ji, Y. Ma, J. Y. Lee and J. M. Lu, *Appl. Mater. Interfaces*, 2011, **3**, 3078-3083.
25. M. J. Allen, V. C. Tung and R. B. Kaner, *Chem. Rev.*, 2010, **110**, 132-145.
26. G. X. Wang, X. P. Shen, J. Yao and J. Park, *Carbon*, 2009, **47**, 2049-2053.
27. K. S. Novoselov, A. K. Geim, S. V. Morozov, D. Jiang, M. I. Katsnelson, I.V. Grigorieva, S. V. Dubonos and A. A. Firsov, *Nature*, 2005, **438**, 197-200.
28. L. B. Chen, M. Zhang and W. F. Wei, *J. Nanomater*, 2013, **2013**, Article ID 937019.
29. M. D. Stoller, S. Park, Y. W. Zhu, Jinho An and R. S. Ruoff, *Nano Lett.*, 2008, **10**, 3498-3502.
30. W. Lv, D. M. Tang, Y. B. He, C. H. You, Z. Q. Shi, X. C. Chen, C. M. Chen, P. X. Hou, C. Liu and Q. H. Yang, *ACS Nano*, 2009, **3**, 3730-3736.
31. P. C. Lian, X. F. Zhu, H. F. Xiang, Z. Li, W. S. Yang and H. H. Wang, *Electrochim. Acta*, 2010, **56**, 834-840.
32. Z. Y. Wang and C. J. Liu, *Nano Energy*, 2015, **11**, 277-293.
33. S. Bai and X. P. Shen, *RSC Adv.*, 2012, **2**, 64-98.
34. C. J. Zhao, S. L. Chou, Y. X. Wang, C. F. Zhou, H. K. Liu and S. X. Dou, *RSC Adv.*, 2013, 3, 16597-16603.
35. X. M. Dong, L. Li, C. J. Zhou, H. K. Liu and Z. P. Guo, *J. Mater. Chem. A*, 2014, **2**, 9844-9850.
36. T. Q. Wang, X. L. Wang, Y. Lu, Q. Q. Xiong, X. Y. Zhao, J. B. Cai, S. Huang, C. D. Gu and J. P. Tu, *RSC Adv.*, 2014, **4**, 322-330.
37. J. S. Zhou, H. H. Song, L. L. Ma and X. H. Chen, *RSC Adv.*, 2011, **1**, 782-791.
38. W. S. Hummers and R. E. Offeman, *J. Am. Chem. Soc.*, 1958, **80**, 1339-1339.
39. L. Stobinski, B. Lesiak, A. Malolepszy, M. Mazurkiewicz, B. Mierzwa, J. Zemek, P. Jiricek and I. Bieloshapka, *J. Electron Spectrosc.*, 2014, **195**, 145-154.
40. W. Wu, X. H. Xiao, S. F. Zhang, H. Li, X. D. Zhou and C. Z. Jiang, *Nanoscale Res. Lett.*, 2009, **4**, 926-931.
41. Y. C. Si and E. T. Samulski, *Nano Lett.*, 2008, **8**, 1679-1682.
42. K. Yang, H. B. Peng, Y. H. Wen and N. Li, *Appl. Surf. Sci.*, 2010, **256**, 3093-3097.
43. C. Nethravathi and M. Rajamathi, *Carbon*, 2008, **46**, 1994-1998.
44. A. C. Ferrari and J. Robertson, *Phys. Rev. B*, 2000, **61**, 14095-14107.
45. M. Zhang, M. Q. Jia and Y. H. Jin, *Appl. Surf. Sci.*, 2012, **261**, 298-305.
46. Y. Q. Zou, J. Kan and Y. Wang, *J. Phys. Chem. C*, 2011, **115**, 20747-20753.
47. C. D. Wang, Q. M. Zhang, Q. H. Wu, T. W. Ng, T. L. Wong, J. G. Ren, Z. C. Shi, C. S. Lee, S. T. Lee and W. J. Zhang, *RSC Adv.*, 2012, **2**, 10680-10688.
48. Q. Y. An, F. Lv, Q. Q. Liu, C. H. Han, K. N. Zhao, J. Z. Sheng, Q. L. Wei, M. Y. Yan and L. Q. Mai, *Nano Lett.*, 2014, **14**, 6250-6256.
49. Y. He, L. Huang, J. S. Cai, X. M. Zheng and S. G. Sun, *Electrochim. Acta*, 2010, **55**, 1140-1144.
50. Y. Z. Wu, R. J. Balakrishna, M. V. Reddy, A. S. Nair, B. V. R. Chowdari and S. Ramakrishna, *J. Alloys Compd.*, 2012, **517**, 69-74.

Figure and table captions

Fig. 1 Schematic illustration for the preparation of Fe_3O_4-rGO composite

Fig. 2 XRD patterns of (a) GO, (b) rGO, (c) pure Fe_3O_4 and (d) Fe_3O_4-rGO composite

Fig. 3 FTIR spectra of (a) graphite, (b) GO and (c) Fe_3O_4-rGO composite

Fig. 4 Raman spectra of (a) GO and (b) Fe_3O_4-rGO composite

Fig. 5 TG profile of (a) rGO, (b) Fe_3O_4-rGO composite and (c) Fe_3O_4

Fig. 6 SEM images of (a) GO, (b) Fe_3O_4 and (c,d) Fe_3O_4-rGO composite

Fig. 7 Photos of rGO and Fe_3O_4-rGO composite dispersed in distilled water before (a) and after (b) treated by a magnet

Fig. 8 Cyclic voltammograms of the Fe_3O_4-rGO electrode at a scan rate of 0.2 $mV \cdot s^{-1}$ for three cycles

Fig. 9 Charge-discharge profiles of (a) Fe_3O_4 and (b) Fe_3O_4-rGO electrodes from first to fifth cycles at a current density of 92.4 $mA \cdot g^{-1}$

Fig. 10 Rate performance of the (a) Fe_3O_4 and (b) Fe_3O_4-rGO electrodes at different current densities

Fig. 11 Cycling performance of (a) Fe_3O_4 and (b) Fe_3O_4-rGO electrodes at a current density of 924 $mA \cdot g^{-1}$ for 50 cycles

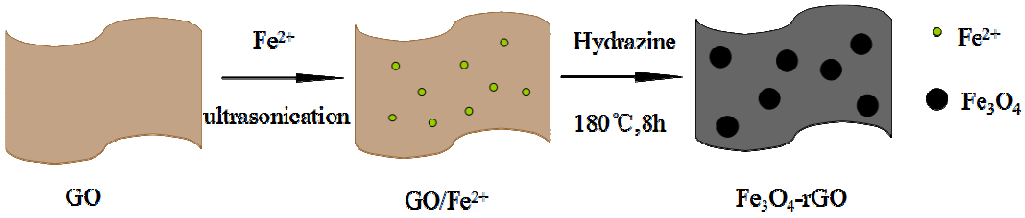

Fig. 1 Schematic illustration for the preparation of Fe_3O_4-rGO composite

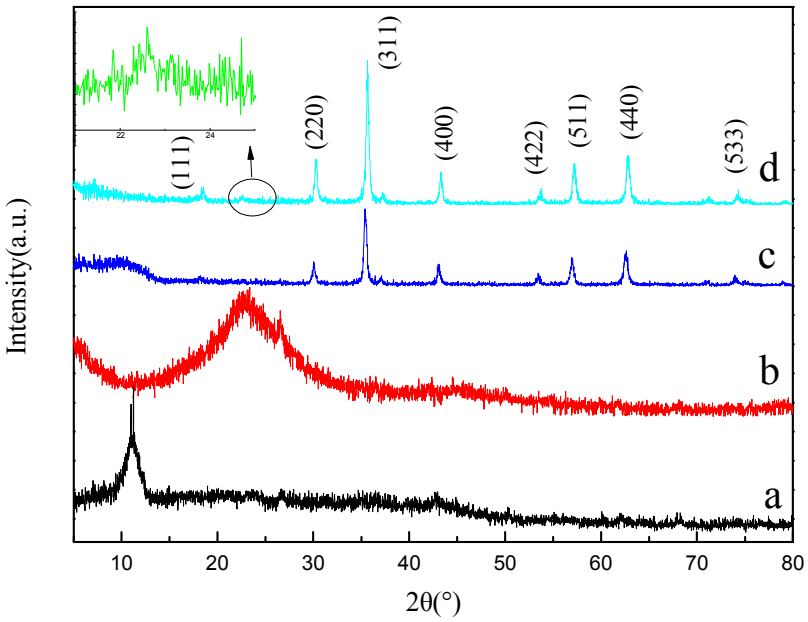

Fig. 2 XRD patterns of (a) GO, (b) rGO, (c) pure Fe_3O_4 and (d) Fe_3O_4-rGO composite

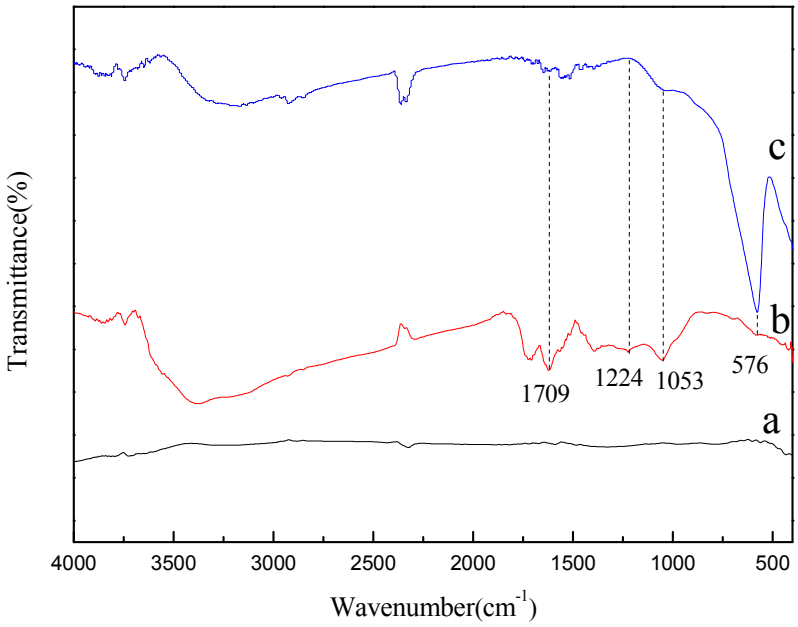

Fig. 3 FTIR spectra of (a) graphite, (b) GO and (c) Fe_3O_4-rGO composite

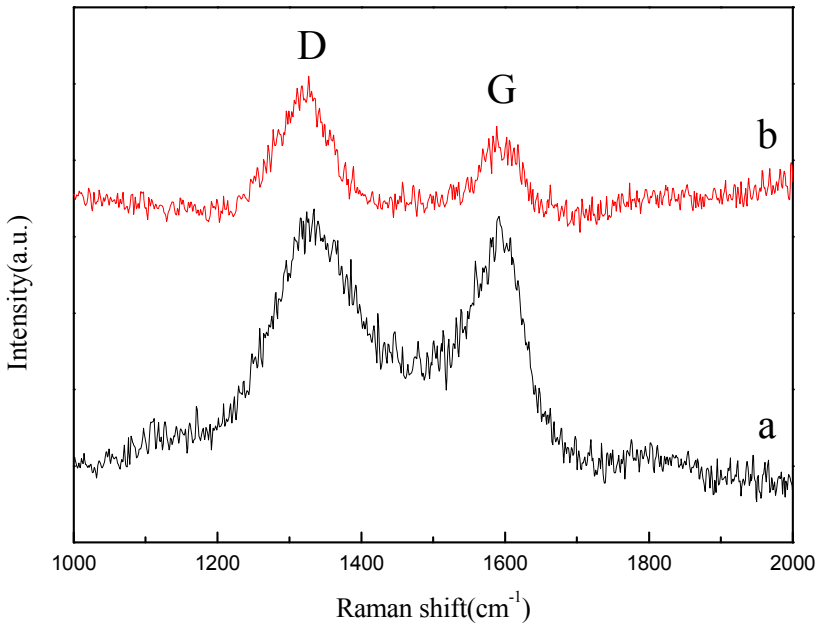

Fig. 4 Raman spectra of (a) GO and (b) Fe_3O_4-rGO composite

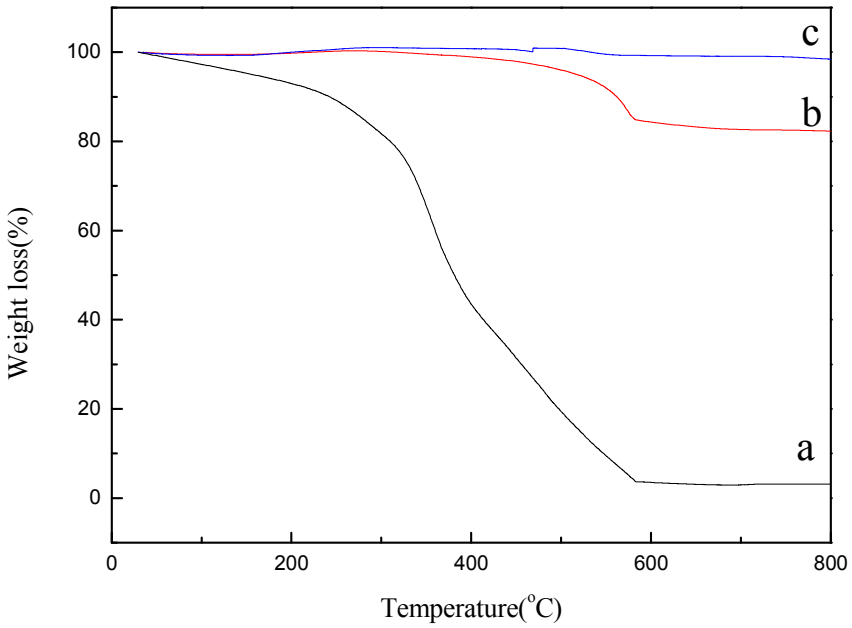

Fig. 5 TG profile of (a) rGO, (b) Fe_3O_4-rGO composite and (c) Fe_3O_4

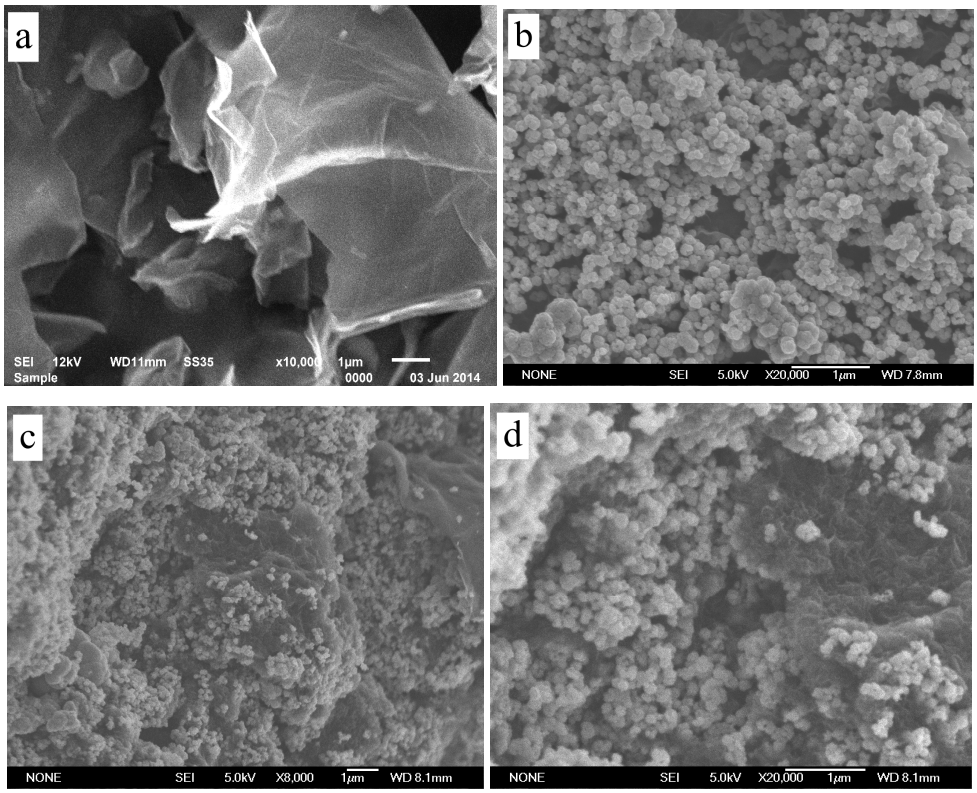

Fig. 6 SEM images of (a) GO, (b) Fe_3O_4 and (c,d) Fe_3O_4-rGO composite

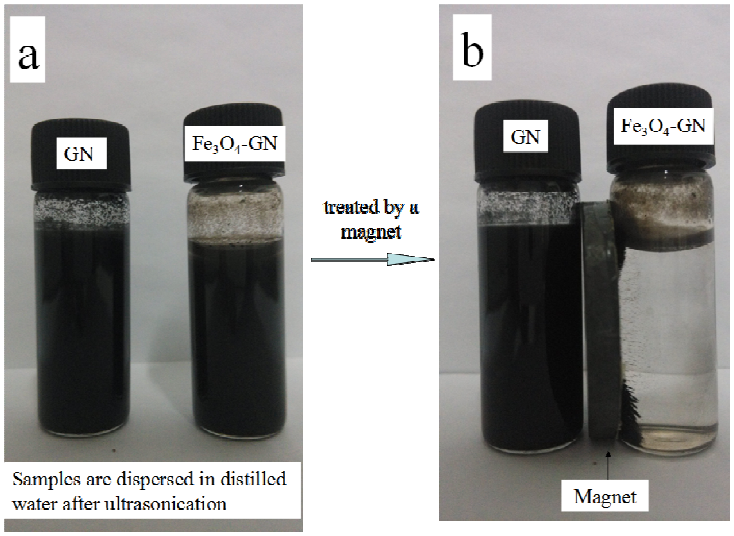

Fig. 7 Photos of rGO and Fe_3O_4-rGO composite dispersed in distilled water before (a) and after (b) treated by a magnet

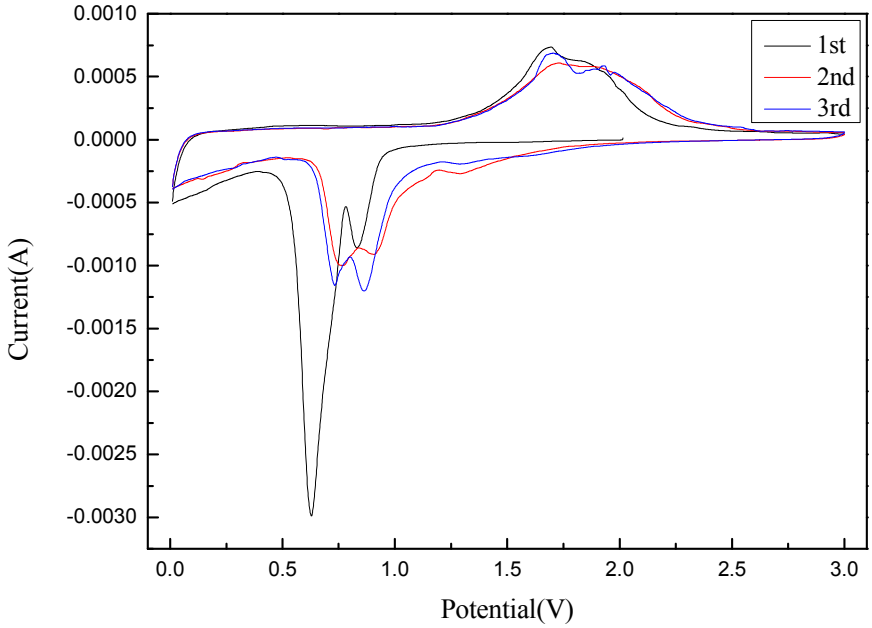

Fig. 8 Cyclic voltammograms of the Fe_3O_4-rGO electrode at a scan rate of 0.2 $mV \cdot s^{-1}$ for three cycles

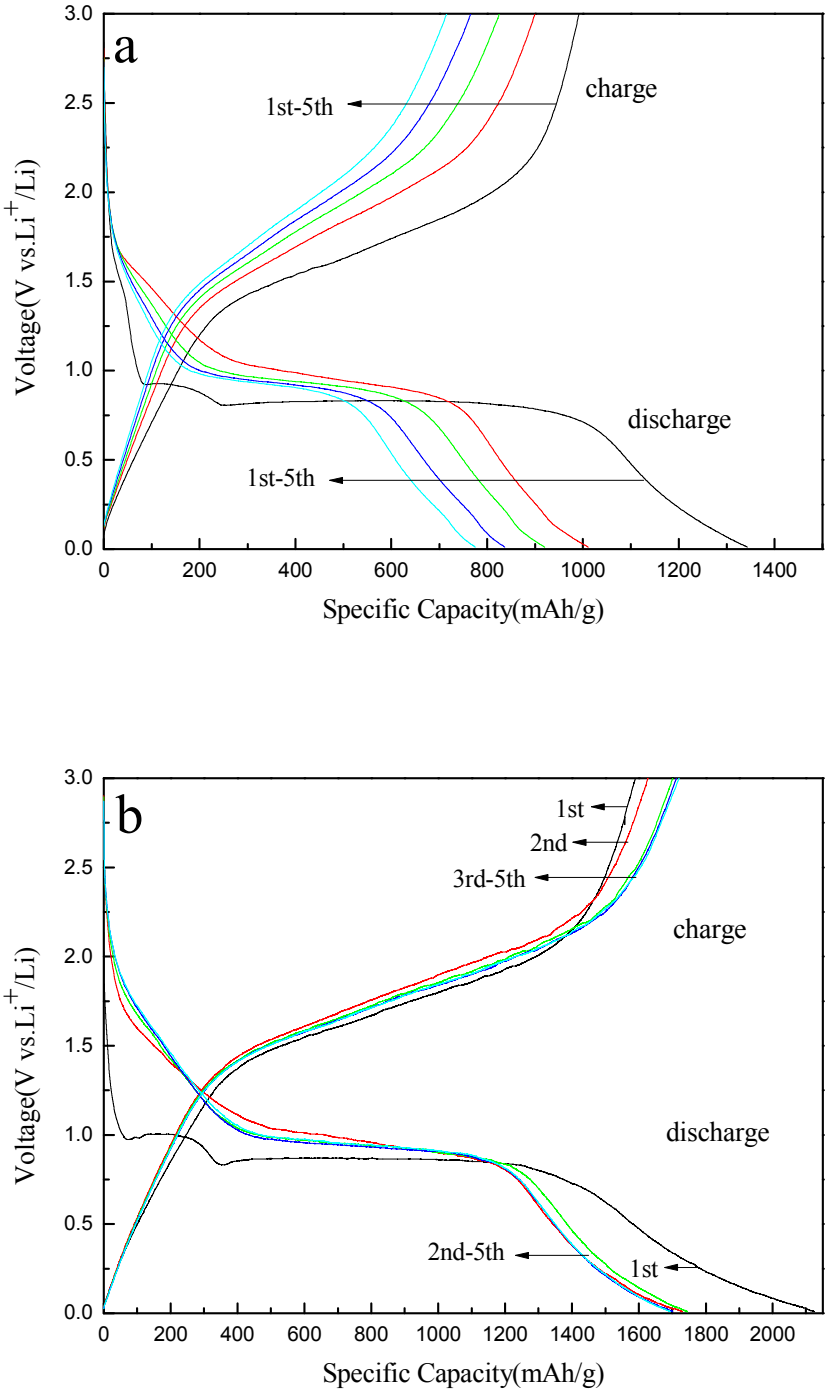

Fig. 9 Charge-discharge profiles of (a) Fe_3O_4 and (b) Fe_3O_4-rGO electrodes from first to fifth cycles at a current density of 92.4 $mA \cdot g^{-1}$

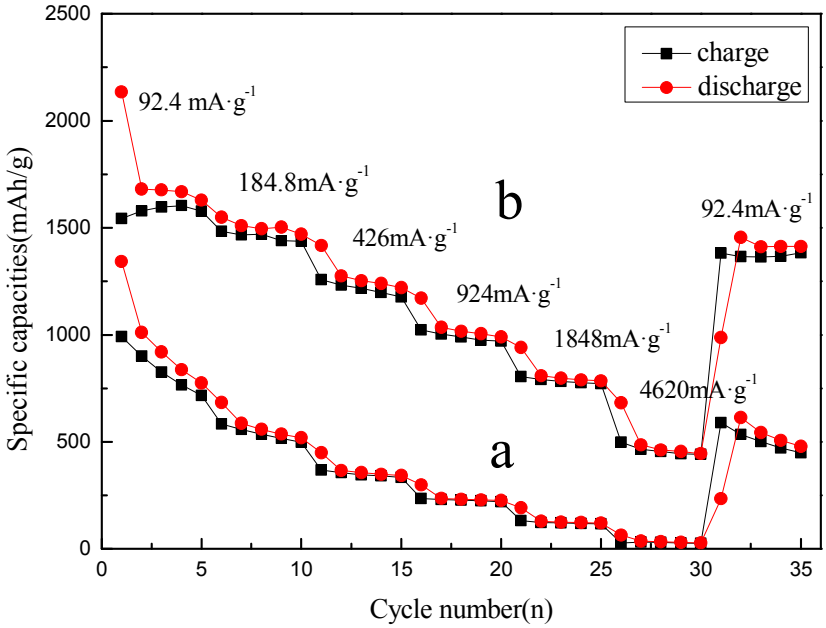

Fig. 10 Rate performance of the (a) Fe_3O_4 and (b) Fe_3O_4-rGO electrodes at different current densities

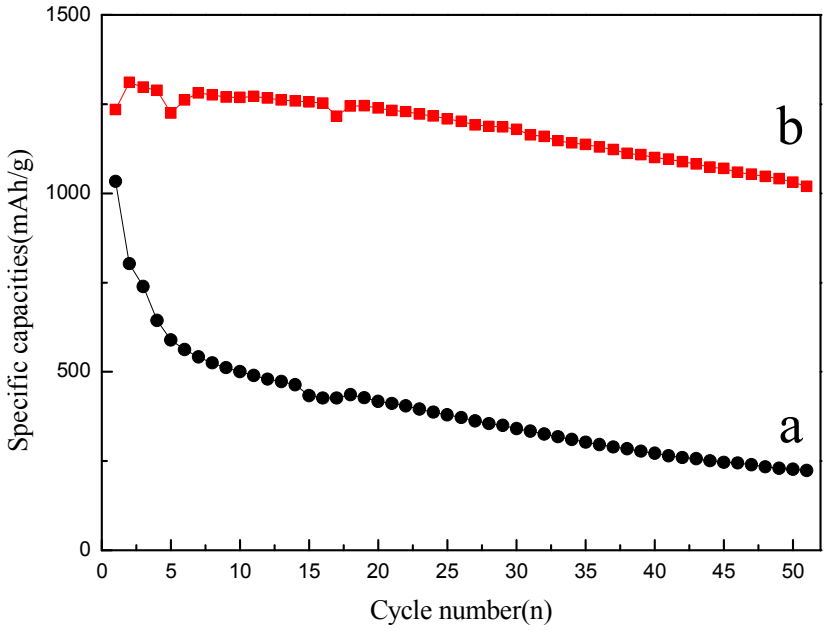

Fig. 11 Cycling performance of (a) Fe_3O_4 and (b) Fe_3O_4-rGO electrodes at a current density of 924 mA·g^{-1} for 50 cycles